



OPEN

A new method of magnetic pulse welding of dissimilar metal plates using a uniform pressure electromagnetic actuator based on pre-deformation

Hang Zhang^{1✉}, Hongfa Ding², Xiaoxiang Li² & Quanliang Cao^{2✉}

The magnetic pulse welding method using a uniform pressure electromagnetic actuator can effectively weld dissimilar metal plates. However, the existing uniform pressure welding method leads to serious thinning of the plate at the chamfer, lack of welding at the center, and bulging of the welded sample, which seriously affects the quality of the welded joint. To solve these problems and improve the quality of welded joints, a new uniform pressure welding method of dissimilar metal plates based on pre-deformation was developed in this work. In this study, using the welding of an AA1060 aluminum plate and an SS304 steel plate with a thickness of 1 mm as an example, it was confirmed through numerical simulation and experimental research that the pre-deformation of the flyer plate controlled the impact angle of the central area of the plate, and it effectively suppressed central non-welding and serious bulge issues. Further, the welding method also reduced the height of the cushion blocks on both sides, thus mitigating aluminum plate thinning at the chamfer, ultimately improving the tensile strength of the joint. Additionally, a microscopic observation showed that the welding interface formed a wavy composite interface, and the connection strength was good. This welding method can also be extended to welding other dissimilar metal plates.

Keywords Magnetic pulse welding, Uniform pressure electromagnetic actuator, Pre-deformation, Welding quality, Wavy composite interface

Lightweight technology is an important means to achieve effective energy conservation, material reduction and environmental protection in many fields such as automobiles, ships, aerospace, household appliances and power electronics^{1,2}. With the premise of ensuring the structural strength of the equipment, one effective means of energy conservation and environmental protection is through reducing the weight of the equipment components, by replacing traditional steel with lightweight and high-strength aluminum alloys, magnesium alloys, and composite materials³. However, when connecting different metals, due to significant differences in their physical and chemical properties, traditional fusion welding may result in heat-affected zones and welding cracks with overheated structures, thus making it difficult to achieve high-quality welding⁴. As a new solid state welding technology, magnetic pulse welding (MPW) drives two metal materials to collide at high speed through electromagnetic force. Under high temperature, high pressure and high strain rates at the collision interface, the metal materials will undergo inter-atomic diffusion to achieve metallurgical bonding between the dissimilar metals^{5,6}. MPW technology has almost no heat-affected zone, a high welding strength, no need for auxiliary materials, and no pollution, and thus can effectively solve the welding problem between dissimilar metals⁷.

According to the structure of the workpiece to be welded, current MPW can be divided into pipe welding and plate welding⁸. MPW of pipe fittings was studied previously; the technology is relatively mature and has industrial applications^{9,10}. Research on MPW of plates started relatively later; the technology is not sufficiently mature, and its application is still in the experimental research stage^{11,12}. According to the differences in the MPW devices and weld morphology, the current MPW process for plates can be summarized into three types:

¹College of Energy Engineering, Huanghuai University, Zhumadian 463000, People's Republic of China. ²Wuhan National High Magnetic Field Center, Huazhong University of Science and Technology, Wuhan 430074, People's Republic of China. ✉email: zhanghang@huanghuai.edu.cn; quanliangcao@mail.hust.edu.cn

(1) magnetic pulse wire welding based on a single-turn wire^{10,13,14}, (2) magnetic pulse spot welding based on a field shaper^{15,16}, and (3) magnetic pulse surface welding based on a uniform pressure electromagnetic actuator (UPEA). Among them, MPW based on a single-turn wire has been studied the most and the technology is relatively mature, and it is currently the most widely used MPW method for plates^{17,18}. However, with the use of a single-turn wire as the driving coil, the device load is smaller, the circuit current is larger¹⁹, the coil is more vulnerable to deformation damage, there is energy loss in the line, and there is low utilization of welding energy; therefore, it is not conducive to industrial applications.

MPW based on a field shaper and a UPEA has adopted multi-turn coils to realize welding of plates by magnetic focusing, which effectively leverages the coils and improves the rate of energy use²⁰. Magnetic pulse welding based on a UPEA can provide a large area of uniform pressure through a combination of multi-turn coils and a conductive channel, which can increase the welding area and be applied to applications in which a larger welding area is required. Wedding et al.²¹ first applied a UPEA to MPW of plates, designed a set of MPW devices, and used a device to complete the welding of aluminum plates. However, through studying the welded samples, it was found that the flyer plate at the chamfer of the cushion block edge produced a thinning phenomenon, resulting in a lower yield strength of the test piece, with the tensile strength of the joint lower than the strength of the base metal. On this basis, Yu et al.²² used the device to weld an AA1060 aluminum plate and a Q235 steel plate, and successfully completed uniform pressure welding (UPW) between the different metals. The welding results under different welding conditions were studied and analyzed, but it was found that the welded samples were not welded in the center and had serious bulging problems, and the problem of thinning at the chamfer of the flyer plate was still present.

To solve the issues of the unwelded center of the welded sample, and bulging and thinning at the chamfer of the flyer plate in UPW, a new method of MPW of dissimilar metal plates using UPEA based on pre-deformation was proposed in this work. The method regulated the collision angle in the center region of the plate through pre-deformation, effectively solved the un-welded center and severe bulging issues by selecting the appropriate pre-deformation height, and also reduced the height of the pad on both sides to reduce thinning of the aluminum plate at the chamfer, thus improving the welding quality of the joint. With the application of lightweight alloy materials in industrial production, the demand for welding between dissimilar metals is also increasing. For example, in the automotive industry, the application of aluminum alloys is becoming increasingly more widespread, which inevitably involves welding an aluminum alloy and steel. This welding method can effectively achieve welding between dissimilar metals and has important industrial application significance. In the next sections, the principles and characteristics, numerical analysis, experimental studies, and microscopic analysis are reported.

Materials and methods

Basic principle of conventional UPW

Figure 1 shows the working principle diagram of traditional uniform pressure welding, including the charging and discharging systems, discharge coil, conductive channel, plate and cushion block. During operation, the conductive channel is fixed to the flyer plate by pressure to form a closed circuit, the coil is placed inside the conductive channel, and the gap between the plates to be soldered can be adjusted by the cushion block. When the capacitor bank finishes charging, it first discharges through the coil to generate a pulse current I_s , followed by an induced eddy current I_c in the closed loop formed by the conductive channel and the flyer plate, and the current generates a strong magnetic field B_c between the closed loop formed by the conductive channel and flyer plate and the coil. Under the joint action of strong magnetic field B_c and induced eddy I_c , the flyer plate will be subjected to a very large electromagnetic repulsive force that produces plastic deformation movement, and it finally collides with the target plate at a high speed to achieve metallurgical bonding to complete the welding process.

According to the principle of MPW, the uniform pressure welding system satisfies the following circuit equation:

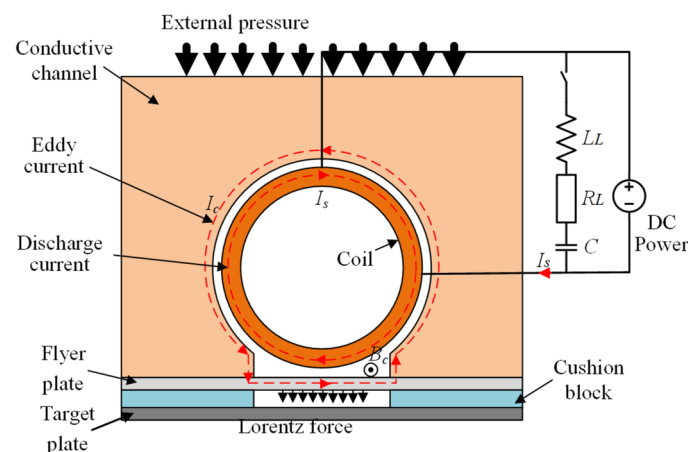


Figure 1. Diagram of the principle of conventional UPW.

$$\frac{dI_s^2}{dt^2} + \frac{R_L + R_{eq}}{L_L + L_{eq}} \frac{dI_s}{dt} + \frac{1}{C(L_L + L_{eq})} I_s = 0 \quad (1)$$

where I_s denotes the circuit discharge current, U_c denotes the capacitor bank voltage, C denotes the discharge capacitance, R_L denotes the line resistance, L_L denotes the line inductance, and R_{eq} and L_{eq} denote the equivalent resistance and equivalent inductance of the coil-conducting channel-flyer plate system, respectively. The discharge loop current shown in Eq. (2) is obtained by solving Eq. (1) according to the initial conditions:

$$I_s = \frac{U_0}{\omega_d(L_L + L_{eq})} e^{-\alpha t} \sin \omega_d t \quad (2)$$

$$\alpha = \frac{R_L + R_{eq}}{2(L_L + L_{eq})} \quad (3)$$

$$\omega_d = \sqrt{\omega_0^2 - \alpha^2} \quad (4)$$

$$\omega_0 = \frac{1}{\sqrt{C(L_L + L_{eq})}} \quad (5)$$

where U_0 denotes the initial discharge voltage; and α , ω_d , and ω_0 denote the attenuation coefficient, attenuation oscillation angle frequency, and resonance angle frequency of the circuit, respectively. The electromagnetic force F on the coil and the flyer plate is determined by the induced eddy current density J and the magnetic flux density B , as shown in the following equation:

$$F = J \times B \quad (6)$$

Magnetic pressure is also an important physical parameter in the MPW process, and the magnetic pressure acting on the surface of the flyer plate can be further expressed as follows:

$$P_M = \frac{B_c^2}{2\mu_0} \quad (7)$$

The flyer plate undergoes plastic deformation motion under the action of electromagnetic force, and its motion satisfies the following equation:

$$\nabla \cdot \sigma + F_v = \rho \frac{\partial^2 u}{\partial t^2} \quad (8)$$

where σ is the stress tensor of the workpiece, F_v is the bulk density vector of the electromagnetic force, ρ is the workpiece density, and u is the displacement vector.

Proposed UPW method based on pre-deformation

The literature²³ showed that the magnetic pressure generated by the UPEA is uniformly distributed in the middle of the deformation region of the flyer plate, which leads to a more uniform force on the corresponding region of the flyer plate; the plastic deformation speed is comparable; and the central region of the flyer plate almost simultaneously collides with the target plate. Although the collision speed is high, the collision angle is nearly zero, and thus it is difficult to form a metallurgical bond; furthermore, due to the collision rebound, the middle of the welding region will form a bulge.

A UPW method based on pre-deformation is proposed in this paper to regulate the collision angle of the plate to be welded, and its schematic diagram is shown in Fig. 2. First, the corresponding welding area of the flyer plate is pre-deformed using a mold to form a slope with a certain height h , as shown in Fig. 2a, to ensure a close fit between the flyer plate and the conductive channel. The width of the pre-deformed area should be slightly smaller than the opening width of the conductive channel. Then the welding experiment is carried out with the pre-deformed flyer plate, as shown in Fig. 2b. Because the corresponding welding area of the flyer plate must be pre-deformed to a certain height, the plastic deformation in the central area of the plate will not be uniform, and the central impact angle will be improved. By changing the height of the pre-deformation, it is possible to adjust the collision angle in the central area of the plate, thus finding the most suitable pre-deformation height and angle, and ultimately improving the welding quality in the central area. In addition, as the flyer plate corresponding to the welding area can be pre-formed at a certain height, the height of the cushion block on both sides can be reduced when the welding gap H remains unchanged, which can also improve the thinning of the plate at the chamfer to a certain extent, and ultimately improve the tensile strength of the welded joint.

Numerical method

To verify the feasibility of the UPW method based on pre-deformation, the commercial software LS-DYNA was used in this study to establish a numerical model of the UPW process. The deformation behavior of the flyer plate during the welding process, the collision angle, and the collision velocity were simulated and analyzed. The geometric model of the UPW device is shown in Fig. 3. The discharge coil was a cylindrical coil, and a

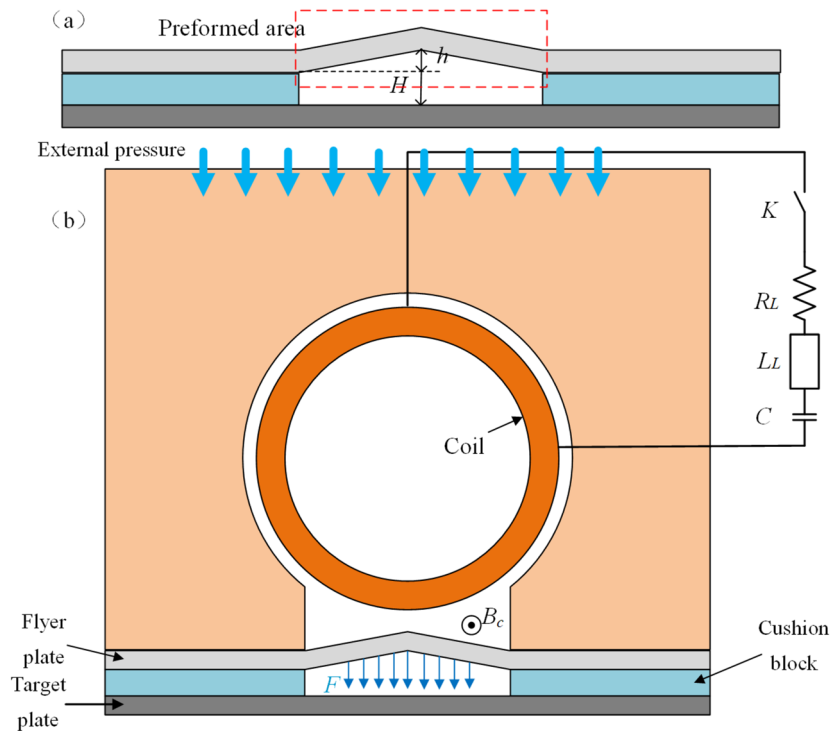


Figure 2. Schematic diagram of the new UPW method.

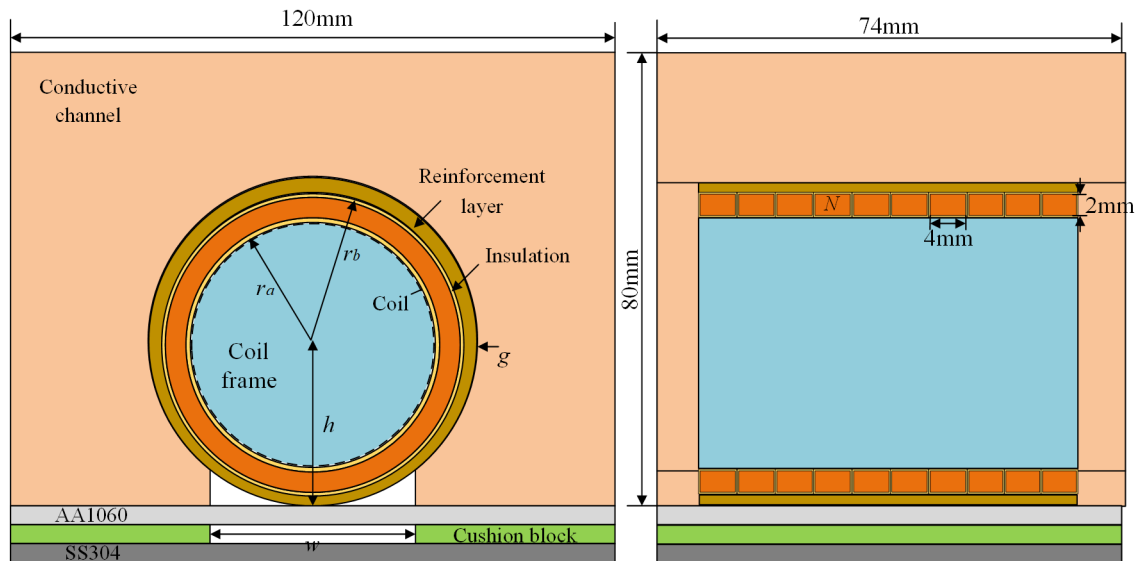


Figure 3. Geometric model of the UPW device.

$4 \times 2 \text{ mm}^2$ square of copper enameled wire was closely wound with a distance between turns of about 0.5 mm. A gap between the coil and the conductive channel was essentially the thickness of the coil wire insulation layer and reinforcement layer. Due to the skin effect, the induced current was mainly distributed on the inner wall of the conductive channel. The external structure of the conductive channel was sized to guarantee its mechanical strength. It had little influence on the eddy current distribution and magnetic pressure, and it was sized here as $120 \times 74 \times 80 \text{ mm}^3$. In addition to the above basic process parameters, the structural parameters, including the number of turns N of the coil, the inner and outer radii r_a and r_b of the coil, respectively, the height of the coil circle h , the opening width w of the conductive channel, and the gap g between the coil and the conductive channel, are shown in Table 1.

Parameters	Description	Value
N	Turns of coil	10
r_a	Inner radius of coil	27 mm
r_b	Outer radius of coil	30 mm
g	Gap	2 mm
w	Opening width of channel	30 mm
h	Height of coil center	32 mm

Table 1. Structural parameters of the UPW device.

To simplify the modeling and save computational time, only the necessary components, such as coils, conductive channel, flyer plates and target plates were selected for modeling the solid mesh, as shown in Fig. 4. The 3D model completely reproduced the welding device used in the actual experimental process.

To simplify the calculation, the current curve of the EMF module was defined by keywords and loaded directly into the 3D model for the solution. Figure 5 shows the experimentally obtained current curve. The flyer plate and target plate were made of an AA1060-O aluminum plate and SS304 stainless steel plate, respectively, both with a thickness of 1 mm. The conductive channel was made of Cu–Cr–Zr with high conductivity and high strength. The electromagnetic and structural parameters of the materials used in the simulation are shown in Tables 2 and 3, respectively.

Considering the high deformation rate of the aluminum plate during welding, a Cowper–Symonds model was selected as a constitutive model of the aluminum plate to characterize the effect of a high strain rate on the high-speed deformation movement of an aluminum plate during welding. The constitutive equation is as follows:

$$\sigma = \sigma_{qs} \left[1 + \left(\frac{\dot{\epsilon}_p^*}{P} \right)^m \right] \quad (9)$$

where σ_{qs} denotes the stress–strain equation for AA1060-O aluminum sheet under quasi-static conditions, $\dot{\epsilon}_p^*$ denotes the strain rate, and P and m denote the constants associated with the inverse and high strain rate effects, respectively, with values of 6500 and 0.25²⁴.

As shown in Fig. 6, the real stress–strain curves of AA1060-O aluminum under quasi-static conditions were tested and fitted using a universal tensile test machine. A power exponential function was used for fitting²⁵, and the stress–strain equation of the AA1060-O aluminum plate under quasi-static conditions was finally obtained as follows:

$$\sigma_{qs} = 122.92\epsilon^{0.247} \quad (10)$$

Finally, it was also necessary to set the contact surface, boundary conditions, and update frequency of the finite elements and boundary elements. The model used two contact surfaces, SURFACE_TO_SURFACE and

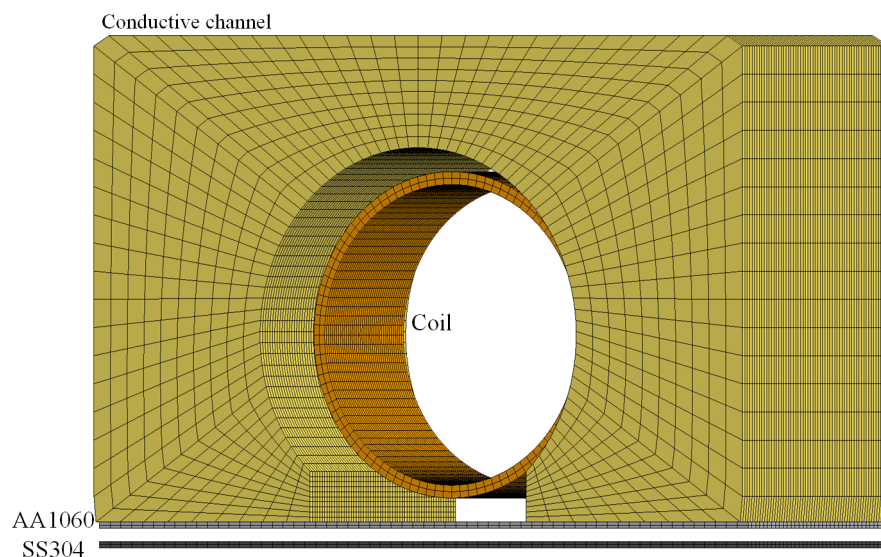


Figure 4. 3D model of the UPW device.

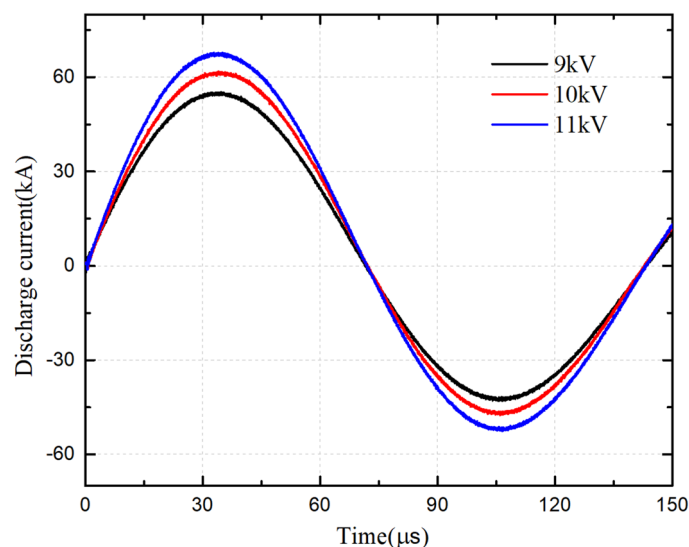


Figure 5. Experimental current curve.

Material types	Resistivity	Permeability
Workpiece		
AA1060-O	3.53×10^7 S/m	$4\pi \times 10^{-7}$ H/m
SS304	1.35×10^6 S/m	$4\pi \times 10^{-7}$ H/m
Coil		
Copper	$5.71 \times e7$ S/m	$4\pi \times 10^{-7}$ H/m
Channel		
CuCrZr	$4.52 \times e7$ S/m	$4\pi \times 10^{-7}$ H/m

Table 2. Electromagnetic parameters used in the simulation.

Material types	Density	Yield stress	Young modules	Poisson ratio
Workpiece				
AA1060-O	2.7×10^3 kg/m ³	35 MPa	80.7 GPa	0.34
SS304	7.93×10^3 kg/m ³	280 MPa	220 GPa	0.25
Coil				
Copper	8.9×10^3 kg/m ³	135 MPa	110 GPa	0.34
Channel				
CuCrZr	8.93×10^3 kg/m ³	495 MPa	117 GPa	0.34

Table 3. Structural parameters used in the simulation.

AUTOMATIC_SURFACE_TO_SURFACE_TIES_WELD, to characterize the solid solution bonding between the two interfaces of the plate after the high-speed collision. First, the former was used to buffer the speed of the plate after high-speed collision, and then the latter was used to form a solid solution for bonding in the collision area to limit the rebound of the plate, to simulate the welding process of two plates under high-speed impact. Selecting the nodes at both ends of the aluminum plate and fixing them with constraints not only ensured the free deformation of the area to be welded, but it also eliminated modeling of the two end pads. The nodes were fixed and constrained on the lower surface of the stainless steel plate to restrict its movement.

Establishment of experimental platform

To ensure the smooth implementation of the experiment, a high-performance UPW device was first developed, and a complete UPW platform was designed and built, including a pulse power supply device and a magnetic device. The pulse power supply device used the existing capacitive power supply in the laboratory, as shown in Fig. 7a. The welding system used three capacitors to discharge in parallel, with a total capacitance of 150 μ F.

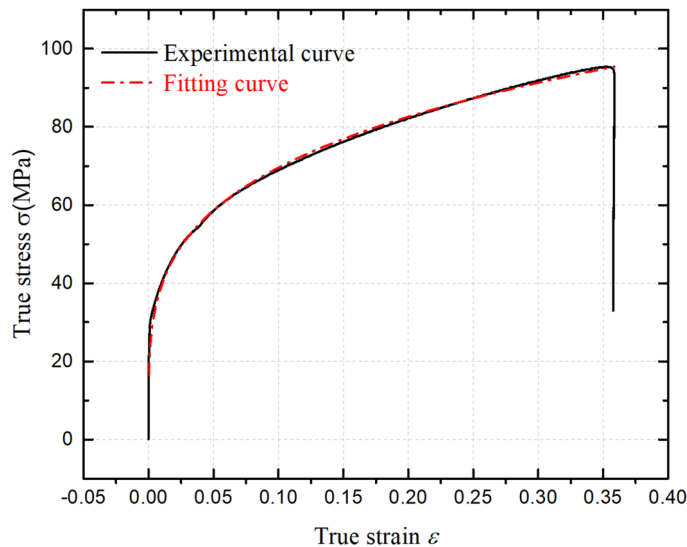


Figure 6. True stress–strain curve of AA1060-O aluminum under quasi-static conditions.

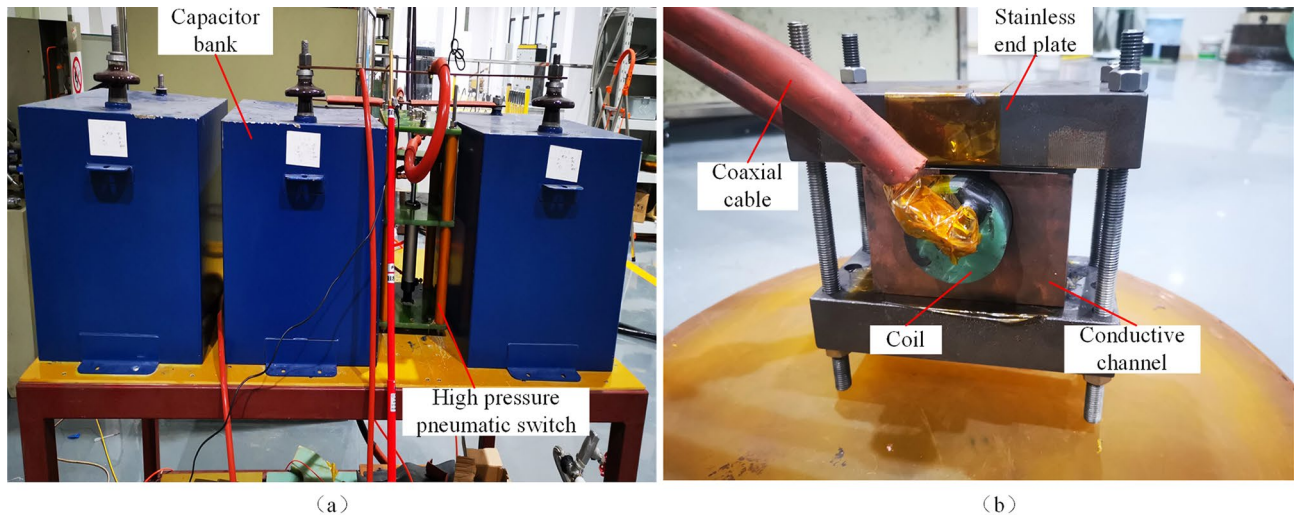


Figure 7. UPW device: (a) pulse power supply device, and (b) magnetic device.

The welding magnetic device is shown in Fig. 7b, in which two stainless steel end plates and bolts were used to reinforce the conductive channels, coils, and plates to provide sufficient pressure during the experiment.

Then, three different sets of pre-deformation molds were designed and made to pre-deform the aluminum plates with heights of 1 mm, 1.5 mm, and 2 mm, as shown in Fig. 8. The aluminum plates to be welded were placed between the molds, and pre-deformation of the plates was achieved by applying pressure. The welding experiments were conducted at 9 kV, 10 kV, and 11 kV for the aluminum plates with different pre-deformation heights at a welding gap of 3 mm²³, and the morphology and mechanical properties of the welded joints were analyzed.

Results and discussion

Numerical verification

First, the feasibility of the UPW method based on pre-deformation was verified using the numerical model established earlier. The deformation behavior, collision angle, and collision velocity of the flyer plate during the welding process were simulated and analyzed.

Effect of pre-deformation on deformation behavior of the flyer plate

Figure 9 shows the simulation results of plastic deformation and the collision process of the aluminum plates welded with preformed heights of 1 mm, and of the undeformed aluminum plates in which the welding gap was 3 mm. Figure 9a shows the plastic deformation process of the aluminum plate without pre-deformation. It can be

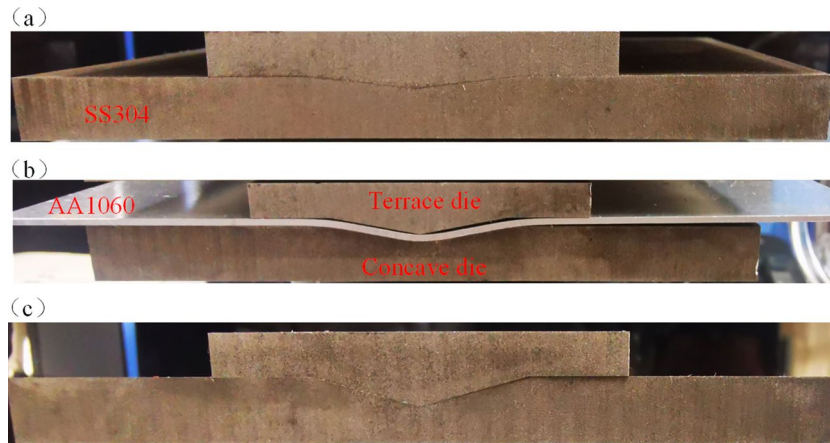


Figure 8. Molds with different pre-deformation height: (a) 1 mm, (b) 1.5 mm, and (c) 2 mm.

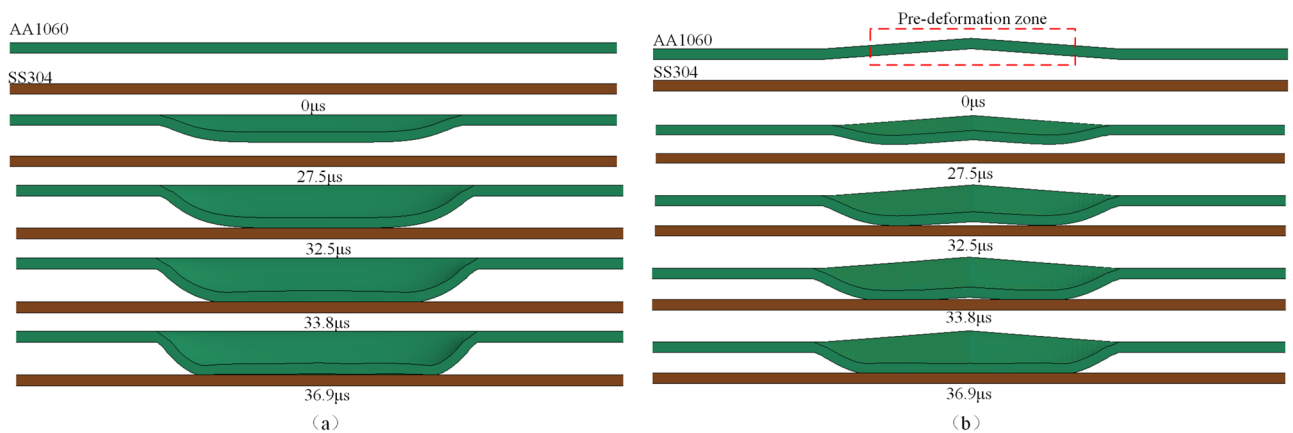


Figure 9. Plastic deformation process of aluminum plate: (a) no pre-deformation, and (b) pre-deformed height of 1 mm.

seen that in the middle position of the welding region, the aluminum plate showed uniform deformation, most of the central region of the aluminum plate almost simultaneously collided with the stainless steel plate, and the collision angle was essentially zero; welding was therefore impossible. After the collision, the aluminum plate rebounded and formed a bulge area. As the collision proceeded, a collision angle only formed at the ends, and therefore the weld channel only formed at the ends, and the center produced an unwelded bulge area. Figure 9b shows the plastic deformation process of the aluminum plate when the pre-deformation height was 1 mm. It can be seen that the deformation of the aluminum plate in the middle of the welding area was no longer uniform, and the aluminum plate on both sides of the center first collided with the stainless steel plate. As the collision proceeded, a certain collision angle was formed in most areas. Due to the symmetry of the collision, the collision angle was zero only in the very narrow area in the center. The impact angle could be adjusted by adjusting the pre-deformation height. When the impact speed and impact angle were appropriate, metallurgical bonding occurred, thus improving the welding effect in the central area of the plate.

Effect of pre-deformation height on collision angle

To intuitively reflect the impact of pre-deformation on the impact angle during welding, the impact angles at different positions of the plate under different pre-deformation heights were extracted, as shown in Fig. 10. It can be seen from the figure that when the aluminum plate was not pre-deformed, the impact angle was almost zero in the part near the center. The impact angle of the aluminum plate was significantly improved after pre-deformation. As the collision proceeded, from the center to both sides, the collision angle showed a trend of first increasing, then decreasing, and then increasing. The collision angle of the area with a large range of centers was in a more appropriate range of collision angles. Compared with no pre-deformation, after pre-deformation, the initial impact point moved from the center to both sides, and the impact angle inside the initial impact point increased with an increase of pre-deformation height, while the impact angle outside the initial impact point decreased with an increase of the pre-deformation height. Therefore, the collision angle can be adjusted by adjusting the height of pre-deformation to improve the welding quality of the central area of the plate.

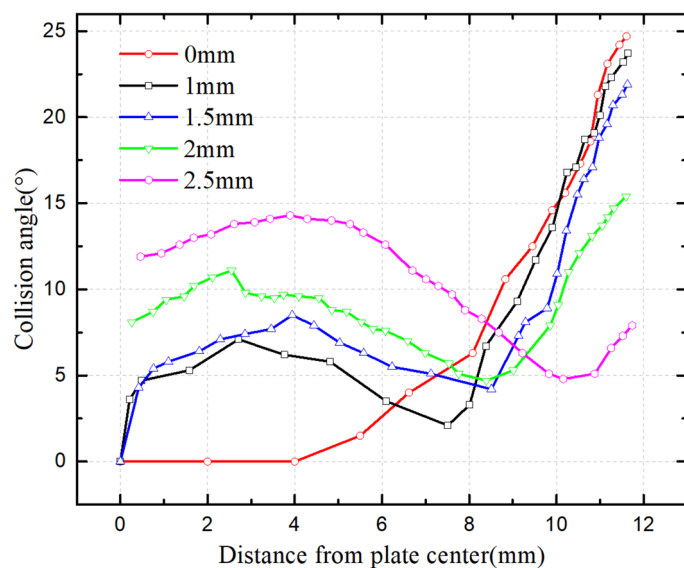


Figure 10. Trend of the collision angle under different pre-deformation heights.

Effect of pre-deformation height on collision velocity

To further analyze the impact of pre-deformation on the welded plates, the curve of maximum impact velocity at different positions of the plates under different pre-deformation heights was generated, as shown in Fig. 11. It can be seen from the figure that when the aluminum plate was not pre-deformed, the collision velocity was basically equal in a large area near the center, which also corresponded to a collision angle in the front area of almost zero. When the aluminum plate was pre-deformed, the impact velocity was no longer uniform, and it showed a decreasing trend from the center to both sides. With an increase of the pre-deformation height, the overall impact velocity decreased. This is because the two sides of the center area collided first after pre-deformation of the aluminum plate, which hindered deformation of the aluminum plate in the center area. Particularly when the pre-deformation height reached 2.5 mm, the impact velocity decreased significantly. In addition, when the maximum collision gap H was held constant, the collision gap at the initial collision position decreased with an increase of the pre-deformation height, which also led to a reduction of the maximum collision speed. To ensure the welding quality, it was necessary to further improve the welding energy.

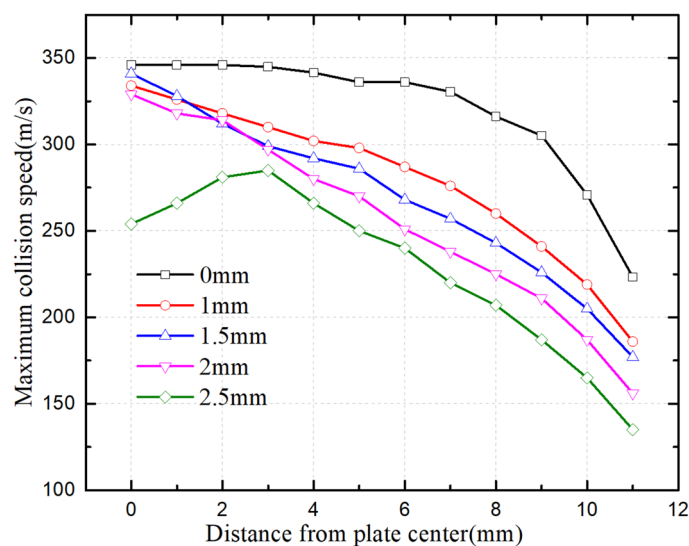


Figure 11. Trend of the maximum collision speed under different pre-deformation heights.

Experimental verification

To further verify the feasibility of the UPW method based on pre-deformation, a series of welding experiments were designed and carried out to study the effect of pre-deformation height and discharge voltage on the morphology of the welded joints.

Effect of pre-deformation height

A sectional view of the welded sample is shown in Fig. 12, along the coil width direction obtained from the welding experiment of the aluminum plates with different pre-deformation heights when the discharge voltage was 10 kV. It can be seen that when the aluminum plate was not pre-deformed, there was a large number of unwelded areas in the center of the welding area, and the central bulge was serious. However, there was only a very narrow gap in the center of the welding area of the welded sample that was welded by the aluminum plate after the pre-deformation treatment, and the unwelded area and bulging phenomenon were significantly improved. In addition, it can be seen from the figure that with an increase of the pre-deformation height, the height of the cushion blocks required at both ends decreased, which effectively reduced the thinning of the aluminum plate at the chamfer. The thickness of the aluminum plate at the chamfer was only 0.5 mm when it was welded without pre-deformation, which was 50% thinner, while the thickness of the aluminum plate at the chamfer was 0.9 mm after pre-deformation of the aluminum plate, which was only 10% thinner. The degree of thinning was drastically reduced, which helped to provide sufficient tensile strength of the joint.

To intuitively reflect the influence of pre-deformation height on the morphology of the weld seam in the welding area, an alkaline solution was used to corrode the welded sample. The black area left after corrosion was the effective welding area, which showed the morphology of the weld seam. The weld bead morphology of samples welded with aluminum plates with different pre-deformation heights under the same voltage are shown in Fig. 13. It can be seen from the figure that when the aluminum plate was not pre-deformed, the weld bead was only formed around the center region because the collision angle in the center of the welding area was almost zero. In the pre-deformed aluminum plates, the collision angle in the center region was improved, a weld bead was formed in the center region, and a wider bead was formed when the pre-deformation height was 1.5 mm.

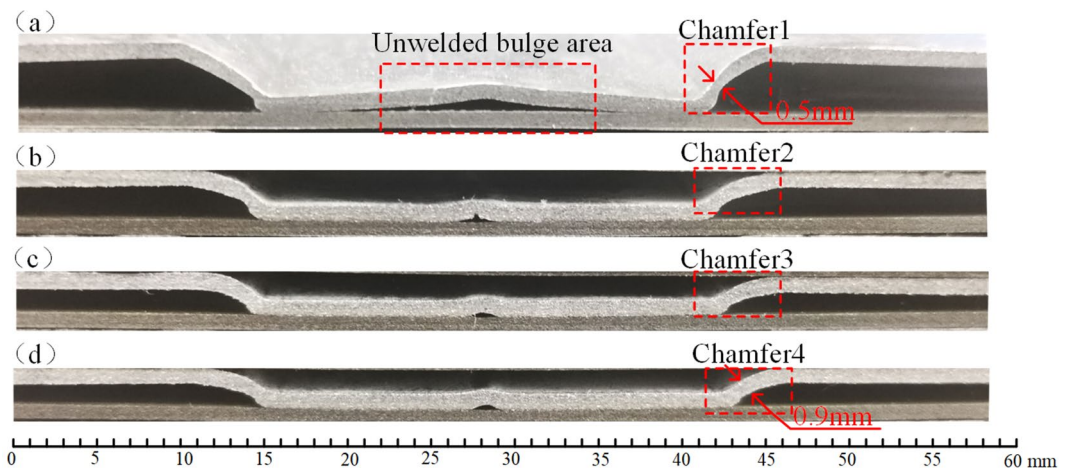


Figure 12. Welded sample section at different pre-deformation heights: (a) 0 mm, (b) 1 mm, (c) 1.5 mm, and (d) 2 mm.

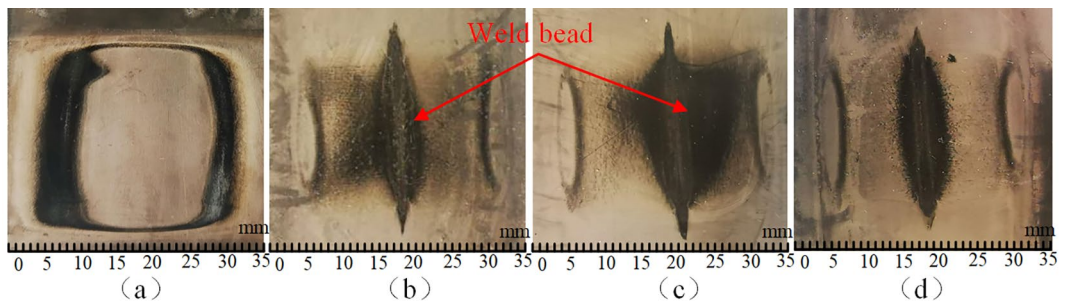


Figure 13. Weld bead morphology of samples at different pre-deformation heights: (a) 0 mm, (b) 1 mm, (c) 1.5 mm, and (d) 2 mm.

To compare the welding effects under different pre-deformation heights, the total welding area and effective welding area of the welded joint were measured and statistically analyzed. The total welding area was the area of the welding outer contour, and the effective welding area was the black area left after alkaline corrosion. The statistical results of the total welding area and effective welding area under different pre-deformation heights are shown in Fig. 14. It can be seen from the figure that with an increase of the pre-deformation height, the total area of the welding area changed little, while the effective welding area showed a trend of first increasing and then decreasing. When the pre-deformation height reached 1.5 mm, the effective welding area was maximized, and the non-welding problem at the center was greatly improved.

According to the simulation analysis, when the pre-deformation height was short, although the impact angle of the central area was improved, the impact angle was still small, and the weld bead was still narrow. As the pre-deformation height increased, the collision angle also increased, and more collision angles entered the appropriate area, forming a wider weld bead in the central area. As the pre-deformation height increased further, the collision velocity also decreased, and it was not possible to form a large weld bead area.

Effect of discharge voltage

Figure 15 shows the cross-section of the welded sample under different discharge voltages when the pre-deformation height was 1.5 mm. It can be seen that with an increase of the discharge voltage, the strip bulge in the center of the welding area had a downward trend. The degree of thinning of the aluminum plate at the chamfer only slightly decreased with an increase of discharge voltage.

To test the bonding strength of the welded joint, a tensile test was carried out on the welded joint, and the tensile displacement curve of the welded joint under different discharge voltages was obtained when the pre-deformation height was 1.5 mm, as shown in Fig. 16. It can be seen from the figure that when the welding voltage was low, the joint was pulled apart. With an increase of discharge voltage, a base metal fracture occurred in the joint, indicating that the tensile strength of the joint was higher than that of the base metal. From the tension-displacement curve of the joint, it can be seen that when the welding voltage reached 11 kV, the maximum tensile strength of the joint exceeded the maximum tensile strength when only the aluminum plate base metal was stretched, indicating that the base metal near the joint had been strengthened to a certain extent. In the

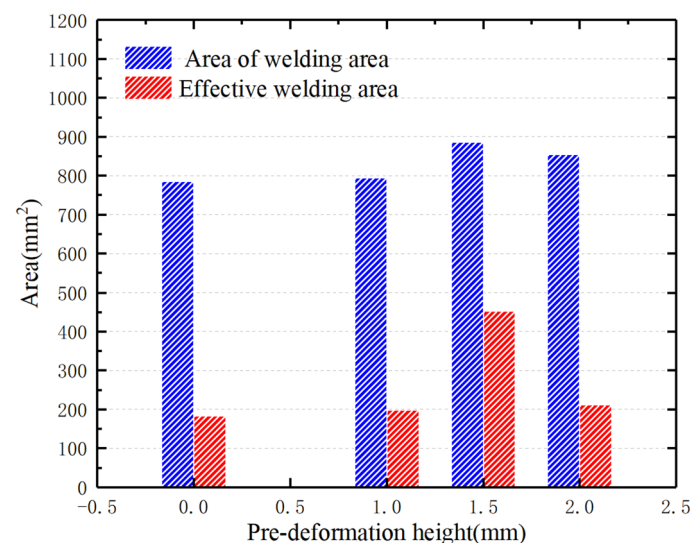


Figure 14. Total welding area and effective welding area at different pre-deformation heights.

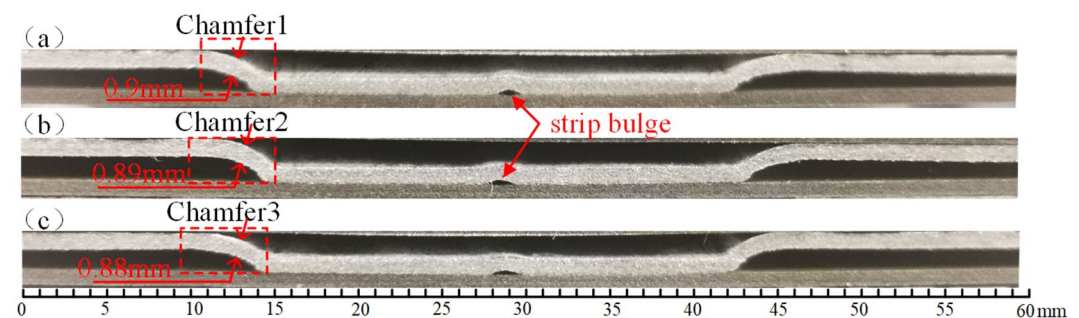


Figure 15. Weld sample section at different discharge voltages: (a) 9 kV, (b) 10 kV, and (c) 11 kV.

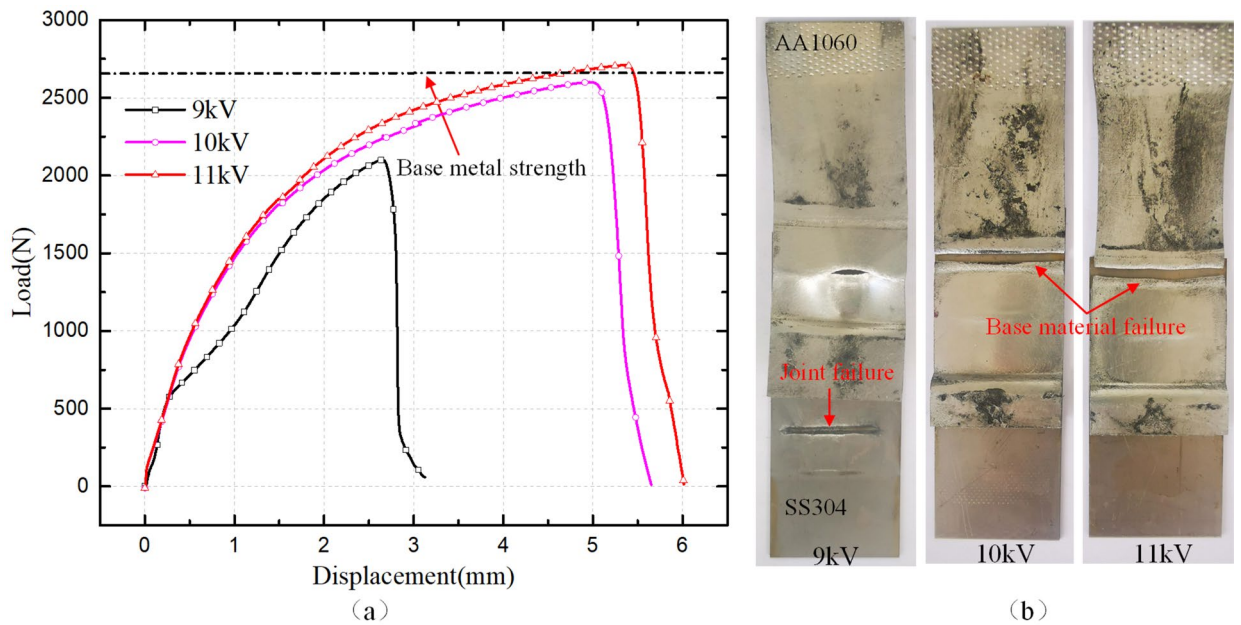


Figure 16. Tensile results: (a) tensile displacement curve, and (b) tensile specimen.

literature²³, the tensile strength of joints obtained by using the undeformed aluminum plate did not reach the strength of the aluminum plate base metal due to thinning of the aluminum plate at the chamfer, which further showed that welding the preformed aluminum plate effectively improved the thinning of the aluminum plate at the chamfer.

As shown in Fig. 17, the weld bead morphology of the welded sample was obtained by using an aluminum plate with a pre-deformation height of 1.5 mm under different discharge voltages. It can be seen that with an increase of discharge voltage, the area of the weld bead in the central area improved. When the discharge voltage reached 11 kV, almost continuous welding of the welding area was achieved.

The statistical results of the total welding area and effective welding area under different discharge voltages are shown in Fig. 18. It can be seen from the figure that with an increase of the discharge voltage, the total area of the welding area increased slowly, while the effective welding area showed a trend of rapid increase. When the discharge voltage reached 11 kV, the effective welding area was close to the total welding area, and the issue with central non-welding had been greatly improved.

Microstructure analysis

To analyze the microstructure of the welded joint, a scanning electron microscope was used to observe the welded interface after polishing. As shown in Fig. 19, the microscopic interface structure of different areas of a welded sample obtained with a pre-deformation height of 1.5 mm and a discharge voltage of 11 kV were observed. The area shown in Fig. 19b was extracted from region 1, and the area shown in Fig. 19c was extracted from region 2. It can be seen that a characteristic waveform interface appeared at both welding interfaces, but changes in the waveform interface differed. In region 1, the interface wave amplitude of the welding interface was small

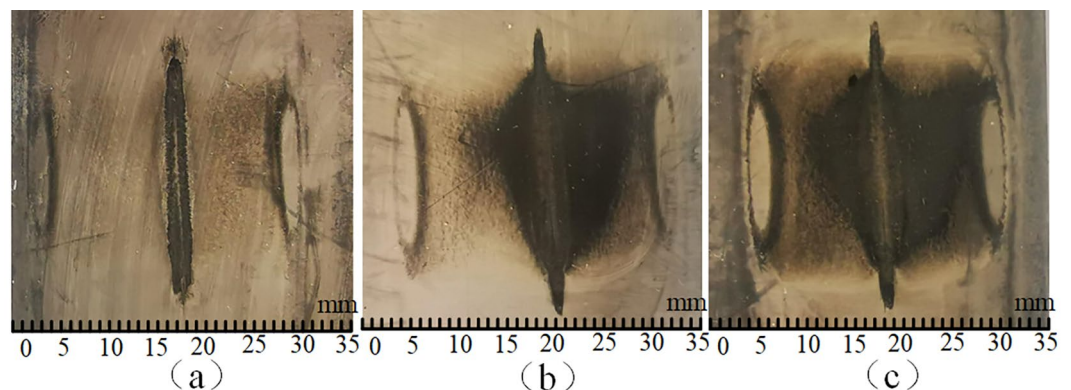


Figure 17. Weld bead morphology of samples at different discharge voltages: (a) 9 kV, (b) 10 kV, and (c) 11 kV.

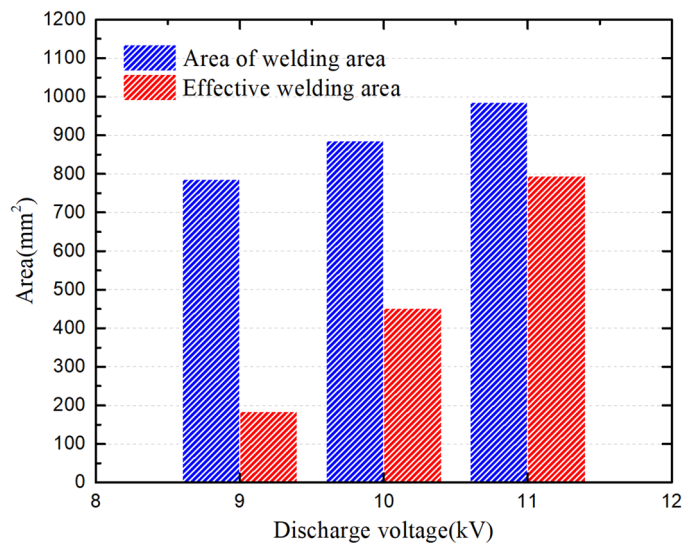


Figure 18. Total welding area and effective welding area at different discharge voltages.

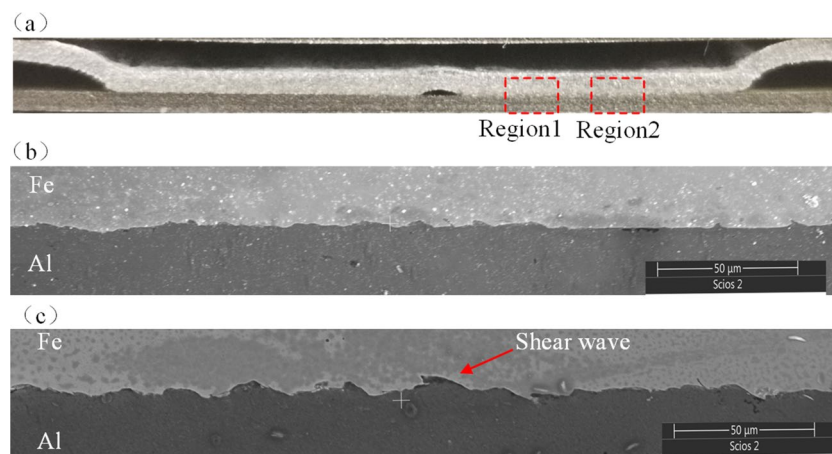


Figure 19. Microscopic interface structure of different areas of the welded sample.

and discontinuous, and there was also a flat interface in the middle. However, in region 2, the amplitude of the interfacial wave at the welding interface was significantly increased and continuous, with shear waves in the middle. The presence of an interfacial wave and the increased amplitude helped to improve the mechanical properties of the welded joints.

In addition, a transition layer was also observed at the welding interface, as shown in Fig. 20. It can be seen that the welding interface produced a clear transition layer. The thickness of the transition layer and the interface wave amplitude were comparable, but the distribution was not uniform, and the thickness was smaller at the interface wave crest. The transition layer was caused by the atomic migration and diffusion of Al and Fe elements on both sides of the welding interface under a large concentration difference and the high temperature and high pressure environment generated by the collision. The presence of an element transition zone also further supported that the magnetic pulse welding metallurgically combined dissimilar metals.

To explore the element distribution characteristics of the welding interface containing the transition layer, an EDS energy spectrum analyzer was used to conduct a line scan of the interface, and the results are shown in Fig. 21. An obvious transition layer can be observed at the welding interface in the figure, and the thickness of the element transition layer reached 7 μm . A small plateau appeared in the element distribution within the transition layer, and the proportion of the two elements in this region was basically unchanged, with the content of Al element slightly higher than that of Fe element. On both sides of the transition layer, the content of both elements decreased rapidly. Within the transition layer, compounds between the two metal elements were usually generated. Intermetallic compounds are generally brittle, and they can easily lead to microcracking; therefore, the thickness of the transition layer should be reduced as much as possible by regulating the welding parameters.

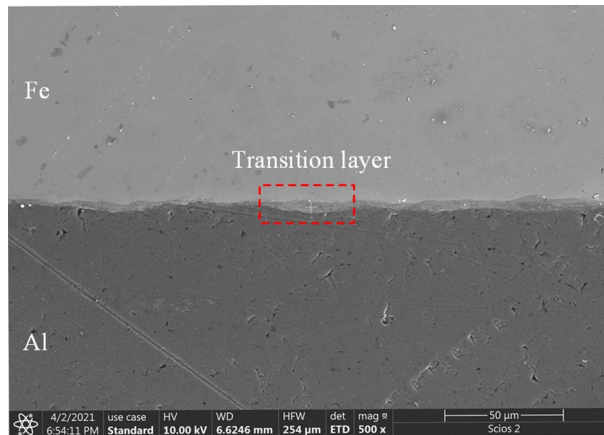


Figure 20. Transition layer at the welding interface.

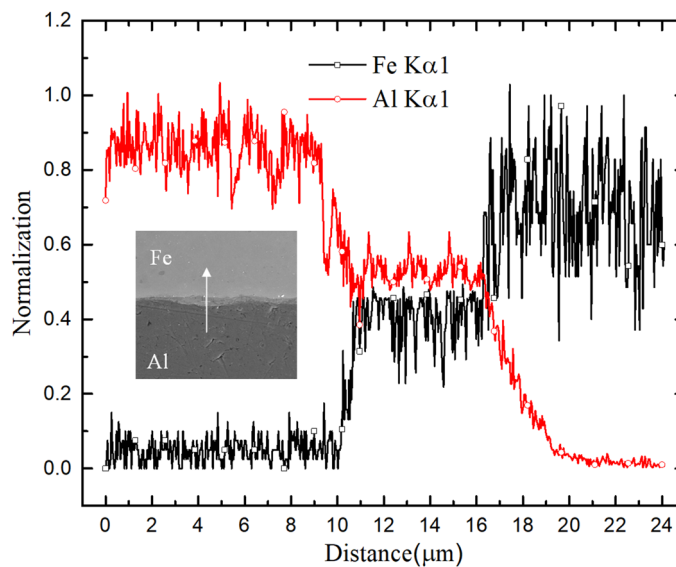


Figure 21. Element distribution in the transition layer.

Conclusion

In this work, with a focus on the issues of an unwelded center, bulging, and chamfer thinning in uniform pressure welding, a new method of magnetic pulse welding of dissimilar metal plates using a uniform pressure electromagnetic actuator based on pre-deformation was proposed. The principles and characteristics of the method were introduced, the feasibility of the method was verified through numerical simulations and experiments, and the microstructure of the welding interface was analyzed in depth. The main results and conclusions are as follows:

- (1) In uniform pressure welding, the impact angle of the plate in the welding center area can be adjusted by pre-deformation of the flyer plate, and the appropriate impact angle can be obtained by selecting the appropriate pre-deformation height h , effectively suppressing the issues of the center not being welded and serious bulging occurring, and thus improving the welding quality of the joints.
- (2) Based on the premise that the maximum welding gap H is not changed, the height of cushion blocks on both sides can be reduced by pre-deformation, which can effectively improve flyer plate thinning at the chamfer, thus improving the welding quality of the joint.
- (3) Under the appropriate welding gap and discharge voltage, the welded joint will form a wavy composite interface, which increases the effective contact area. The formation of the wavy composite interface causes the two metal materials to form an interlocking effect at the interface, which is helpful for improving the mechanical properties of the welded joint.
- (4) This welding method can effectively suppress bulging and thinning through pressure equalization welding, thus improving the welding performance of joints, and has important value and practical significance for

welding dissimilar metals in industrial production. Particularly in the automotive industry, the application of aluminum alloys increasingly involves welding of aluminum alloys and steel.

Data availability

The data required to support the present findings are present in the manuscript and supplementary information.

Received: 29 April 2024; Accepted: 22 July 2024

Published online: 26 July 2024

References

- Liu, N. *et al.* A comparative study on the effects of boundary constraints on electromagnetic sheet forming. *Int. J. Adv. Manuf. Tech.* **101**(9–12), 2785–2793. <https://doi.org/10.1007/s00170-018-3098-z> (2019).
- Qiu, L. *et al.* Construction and analysis of two-dimensional axisymmetric model of electromagnetic tube bulging with field shaper. *IEEE Access.* **8**, 113713–113719. <https://doi.org/10.1109/ACCESS.2020.3003740> (2020).
- Psyk, V., Risch, D., Kinsey, B. L., Tekkaya, A. E. & Kleiner, M. Electromagnetic forming—A review. *J. Mater. Process. Tech.* **211**(5), 787–829 (2011).
- Li, Z., Peng, W., Chen, Y., Liu, W. & Zhang, H. Simulation and experimental analysis of Al/Ti plate magnetic pulse welding based on multi-seams coil. *J. Manuf. Process.* **83**, 290–299. <https://doi.org/10.1016/j.jmapro.2022.09.015> (2022).
- Kore, S. D., Date, P. P. & Kulkarni, S. V. Electromagnetic impact welding of aluminum to stainless steel sheets. *J. Mater. Process. Tech.* **208**(1), 486–493 (2008).
- Manogaran, A. P., Manoharan, P., Priem, D., Marya, S. & Racineux, G. Magnetic pulse spot welding of bimetals. *J. Mater. Process. Tech.* **214**(6), 1236–1244 (2014).
- Lee, K., Kumai, S., Arai, T. & Aizawa, T. Interfacial microstructure and strength of steel/aluminum alloy lap joint fabricated by magnetic pressure seam welding. *Mater. Sci. Eng. A.* **471**(1–2), 95–101. <https://doi.org/10.1016/j.msea.2007.04.033> (2007).
- Lueg-Althoff, J. *et al.* Influence of the flyer kinetics on magnetic pulse welding of tubes. *J. Mater. Process. Tech.* **262**, 189–203. <https://doi.org/10.1016/j.jmatprotec.2018.06.005> (2018).
- Cui, J. *et al.* Joining of tubular carbon fiber-reinforced plastic/aluminum by magnetic pulse welding. *J. Mater. Process. Tech.* **264**, 273–282. <https://doi.org/10.1016/j.jmatprotec.2018.09.018> (2019).
- Chen, S. & Jiang, X. Microstructure evolution during magnetic pulse welding of dissimilar aluminum and magnesium alloys. *J. Manuf. Process.* **19**, 14–21. <https://doi.org/10.1016/j.jmapro.2015.04.001> (2015).
- Kore, S. D., Date, P. P. & Kulkarni, S. V. Effect of process parameters on electromagnetic impact welding of aluminum sheets. *Int. J. Impact. Eng.* **34**(8), 1327–1341. <https://doi.org/10.1016/j.ijimpeng.2006.08.006> (2007).
- Wang, P. Q. *et al.* Electromagnetic pulse welding of al/cu dissimilar materials: Microstructure and tensile properties. *Mater. Sci. Eng. A.* **792**, 139842. <https://doi.org/10.1016/j.msea.2020.139842> (2020).
- Wang, S. *et al.* Mechanical properties and interfacial microstructures of magnetic pulse welding joints with aluminum to zinc-coated steel. *Mater. Sci. Eng. A.* **788**, 139425. <https://doi.org/10.1016/j.msea.2020.139425> (2020).
- Geng, H., Xia, Z., Zhang, X., Li, G. & Cui, J. Microstructures and mechanical properties of the welded aa5182/hc340la joint by magnetic pulse welding. *Mater. Charact.* **138**, 229–237. <https://doi.org/10.1016/j.matchar.2018.02.018> (2018).
- Deng, F., Cao, Q., Han, X. & Li, L. Electromagnetic pulse spot welding of aluminum to stainless steel sheets with a field shaper. *Int. J. Adv. Manuf. Tech.* **98**(5–8), 1903–1911. <https://doi.org/10.1007/s00170-018-2208-2> (2018).
- Zhang, H., Liu, N., Li, X., Deng, F. & Ding, H. A novel field shaper with slow-varying central hole for electromagnetic pulse welding of sheet metal. *Int. J. Adv. Manuf. Tech.* **108**(7–8), 2595–2606 (2020).
- Geng, H., Mao, J., Zhang, X., Li, G. & Cui, J. Strain rate sensitivity of Al-Fe magnetic pulse welds. *J. Mater. Process. Tech.* **262**, 1–10. <https://doi.org/10.1016/j.jmatprotec.2018.06.021> (2018).
- Cui, J. *et al.* Effect of surface treatment on the mechanical properties and microstructures of Al-Fe single-lap joint by magnetic pulse welding. *Int. J. Adv. Manuf. Tech.* **98**(5–8), 1081–1092. <https://doi.org/10.1007/s00170-018-2262-9> (2018).
- Ghosh, P., Patra, S., Chatterjee, S. & Shome, M. Microstructural evaluation of magnetic pulse welded plain carbon steel sheets. *J. Mater. Process. Tech.* **254**, 25–37. <https://doi.org/10.1016/j.jmatprotec.2017.11.012> (2018).
- Zhang, H., Wang, Q., Wang, G. & Ding, H. Analytical modeling and optimization design of an electromagnetic pulse welding device with a field shaper for metal plates. *IEEE Access.* **8**, 187721–187729. <https://doi.org/10.1109/ACCESS.2020.3030909> (2020).
- Weddeling, C., Hahn, M., Daehn, G. S. & Tekkaya, A. E. Uniform pressure electromagnetic actuator—An innovative tool for magnetic pulse welding. *Proc. CIRP.* **18**, 156–161. <https://doi.org/10.1016/j.procir.2014.06.124> (2014).
- Yu, H. & Tong, Y. Magnetic pulse welding of aluminum to steel using uniform pressure electromagnetic actuator. *Int. J. Adv. Manuf. Tech.* **91**(5–8), 2257–2265. <https://doi.org/10.1007/s00170-016-9928-y> (2017).
- Zhang, H., Liu, N., Li, X., Wang, Q. & Ding, H. Optimization design and experimental research of magnetic pulse welding system based on uniform pressure electromagnetic actuator. *Int. J. Adv. Manuf. Tech.* **121**(11–12), 8447–8465. <https://doi.org/10.1007/s00170-022-09797-7> (2022).
- Kim, J. H., Kim, D. & Lee, M. Experimental and numerical analysis of a rectangular helical coil actuator for electromagnetic bulging. *Int. J. Adv. Manuf. Tech.* **78**(5–8), 825–839. <https://doi.org/10.1007/s00170-014-6680-z> (2015).
- Park, J., Kim, J., Kim, K. & Kang, B. Numerical and experimental study of stretching effect on flexible forming technology. *Int. J. Adv. Manuf. Tech.* **73**(9–12), 1273–1280. <https://doi.org/10.1007/s00170-014-5859-7> (2014).

Acknowledgements

We thank LetPub (www.letpub.com) for its linguistic assistance during the preparation of this manuscript.

Author contributions

H.D. and Q.C. supervised the team activity. All authors contributed to the study's conception and design. Material preparation, data collection, and analysis were performed by H.Z. and X.L. The first draft of the manuscript was written by H.Z. and all authors commented on previous versions of the manuscript. All authors read and approved the final manuscript.

Funding

This work was supported by the Natural Science Foundation of Henan province (Grant Numbers 222300420239), also supported by the National Natural Science Foundation of China (Grant Numbers 51821005).

Competing interests

The authors declare no competing interests.

Additional information

Supplementary Information The online version contains supplementary material available at <https://doi.org/10.1038/s41598-024-68191-3>.

Correspondence and requests for materials should be addressed to H.Z. or Q.C.

Reprints and permissions information is available at www.nature.com/reprints.

Publisher's note Springer Nature remains neutral with regard to jurisdictional claims in published maps and institutional affiliations.



Open Access This article is licensed under a Creative Commons Attribution-NonCommercial-NoDerivatives 4.0 International License, which permits any non-commercial use, sharing, distribution and reproduction in any medium or format, as long as you give appropriate credit to the original author(s) and the source, provide a link to the Creative Commons licence, and indicate if you modified the licensed material. You do not have permission under this licence to share adapted material derived from this article or parts of it. The images or other third party material in this article are included in the article's Creative Commons licence, unless indicated otherwise in a credit line to the material. If material is not included in the article's Creative Commons licence and your intended use is not permitted by statutory regulation or exceeds the permitted use, you will need to obtain permission directly from the copyright holder. To view a copy of this licence, visit <http://creativecommons.org/licenses/by-nc-nd/4.0/>.

© The Author(s) 2024